Mohsen, A., Asch, G., Mechie, J., Weber, M., Stiller, M., Hofstetter, R., Abu-Ayyash, K. (2011): Crustal structure of the Dead Sea Basin (DSB) from a Receiver Function Analysis. - Geophysical Journal International, 184, 1, pp. 463—476.

DOI: http://doi.org/10.1111/j.1365-246X.2010.04853.x

Geophysical Journal International

Geophys. J. Int. (2011) **184,** 463–476 doi: 10.1111/j.1365-246X.2010.04853.x

Crustal structure of the Dead Sea Basin (DSB) from a receiver function analysis

A. Mohsen,[1,2] G. Asch,[1,3] J. Mechie,[1] R. Kind,[1,3] R. Hofstetter,[4] M. Weber,[1,5] M. Stiller[1] and K. Abu-Ayyash[1,6]

[1]*Deutsches GeoForschungsZentrum-GFZ, Telegrafenberg,* 14473 *Potsdam, Germany. E-mail: ayman@gfz-potsdam.de*
[2]*Al-Najah National University, Nablus, Palestine*
[3]*Freie Universität, Berlin, Germany*
[4]*Geophysical Institute, Lod, Israel*
[5]*Institut für Geowissenschaften, Universität Potsdam, Potsdam, Germany*
[6]*Natural Resources Authority, Amman, Jordan*

Accepted 2010 October 14. Received 2010 October 12; in original form 2009 December 2

SUMMARY

The Dead Sea Transform (DST) is a major left-lateral strike-slip fault that accommodates the relative motion between the African and Arabian plates, connecting a region of extension in the Red Sea to the Taurus collision zone in Turkey over a length of about 1100 km. The Dead Sea Basin (DSB) is one of the largest basins along the DST. The DSB is a morphotectonic depression along the DST, divided into a northern and a southern sub-basin, separated by the Lisan salt diapir. We report on a receiver function study of the crust within the multidisciplinary geophysical project, DEad Sea Integrated REsearch (DESIRE), to study the crustal structure of the DSB. A temporary seismic network was operated on both sides of the DSB between 2006 October and 2008 April. The aperture of the network is approximately 60 km in the E–W direction crossing the DSB on the Lisan peninsula and about 100 km in the N–S direction. Analysis of receiver functions from the DESIRE temporary network indicates that Moho depths vary between 30 and 38 km beneath the area. These Moho depth estimates are consistent with results of near-vertical incidence and wide-angle controlled-source techniques. Receiver functions reveal an additional discontinuity in the lower crust, but only in the DSB and west of it. This leads to the conclusion that the internal crustal structure east and west of the DSB is different at the present-day. However, if the 107 km left-lateral movement along the DST is taken into account, then the region beneath the DESIRE array where no lower crustal discontinuity is observed would have lain about 18 Ma ago immediately adjacent to the region under the previous DESERT array west of the DST where no lower crustal discontinuity is recognized.

Key words: Transform faults; Crustal structure.

INTRODUCTION

The Dead Sea Basin (DSB) is located within the Dead Sea Transform (DST) which is one of the most significant geological structures in the Middle East and is responsible for most of the recent structures in the region (Quennell 1958; Abou-Karaki 1987).

The DST separates the Arabian and African plates (Fig. 1). It strikes in an NNE direction and extends over some 1100 km from the Red Sea where seafloor spreading occurs, through Wadi Araba, the Dead Sea, the Jordan Valley, Lake Tiberias and central Lebanon to the continental collision zone in the Taurus-Zagros mountain belt (Quennell 1958; El-Isa 1990; Girdler 1990). The DST is generally attributed to a left-lateral shear, which started in the Miocene, and now has a cumulative lateral displacement of 107 km (Quennell 1958; Garfunkel 1981).

The DST is a first-order structure in the Middle East. It is the main source of earthquakes in this region. Large earthquakes are known to have occurred along this structure during the historical period (Abou-Karaki 1987; Ambraseys *et al*. 1994). The internal structure of the transform is dominated by left-stepping en-echelon strike-slip faults (Garfunkel 1981; Garfunkel *et al*. 1981). This fault arrangement produced several pull-apart structures (rhomb-shaped grabens), which form deep basins. The largest of these structures is the DSB, with a total length of 150 km. It is one of the largest and most studied pull-apart basins worldwide (e.g. Kashia & Croker 1987; Garfunkel & Ben-Avraham 1996; Al-Zoubi *et al*.

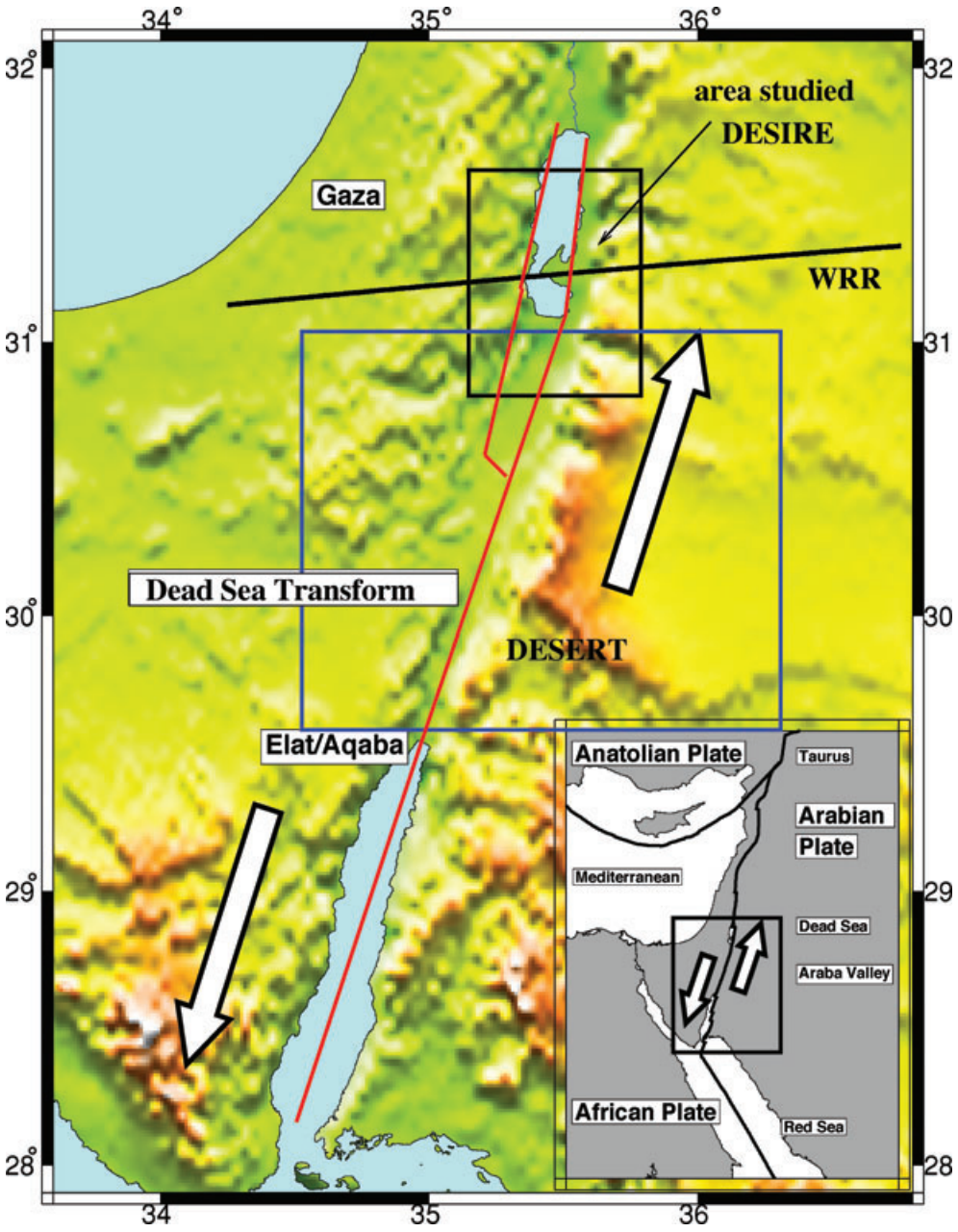

Figure 1. Tectonic map, showing the area studied and the wide-angle reflection/refraction (WRR) profile across the Dead Sea Basin (Mechie *et al*. 2009). The blue box shows the area studied during the DESERT project (DESERT Group 2004; Mohsen *et al*. 2005). The inset shows the regional tectonic setting of the Dead Sea Transform.

2002; Larsen *et al*. 2002; Enzel *et al*. 2006; ten Brink *et al*. 2006; Smit *et al*. 2008). The longitudinal faults bordering the pull-apart basin are the continuation of the major strike-slip faults north and south of the basin (Garfunkel & Ben-Avraham 1996).

The DSB is divided into a northern sub-basin and a southern sub-basin, separated by the Lisan salt diapir (Neev & Hall 1979). The northern sub-basin is covered by the Dead Sea, which is one of the most saline lakes in the world. Its waters contain >30 per cent of dissolved salts, mainly Mg, Na and Ca chlorides as well as high concentrations of K and Br. The southern segment extends northwards from the middle of the Araba valley. Two large salt diapirs have been formed, namely the Lisan and Sedom diapirs. The basin reaches a maximum depth of 8.5 km or more in its central part under the Lisan diapir, as indicated by depth conversion of seismic lines (Al-Zoubi & ten Brink 2001).

Gravity data indicate a large negative anomaly, the largest in the Middle East, over the Lisan peninsula and the southern sub-basin (ten Brink *et al*. 1993, 1999), where the main faults overlap. Modelling of the gravity data has suggested that the southern part of the northern sub-basin has about 9 km of sedimentary fill, overlying a layer about 7 km thick of Mesozoic carbonate platform rocks (ten Brink *et al*. 1993, 1999). More recent gravity modelling (Al-Zoubi & ten Brink 2001) has suggested that the deepest part of the basin is centred under the Lisan peninsula where the basin is about 10 km thick. Magnetic modelling has suggested that 6 km of sedimentary fill overlies about 7 km of Mesozoic carbonates in

the northern sub-basin (Frieslander & Ben-Avraham 1989). Seismic reflection/refraction data indicate that the Precambrian crystalline basement is 12–15 km deep below the southern DSB (Ginzburg & Ben-Avraham 1997). The southern DSB is unusually deep, with about 10 km of sedimentary fill associated with the DST (Ben-Avraham & Schubert 2006).

Petrunen and Sobolev (2006) estimate the maximum depth of the sedimentary fill in most of the DSB to be 8–12 km, with up to 15 km at 31.3°N. At this latitude, the maximum seismicity, which is observed at a depth of 20–22 km beneath most of the basin, reaches 27 km depth (Alderson *et al*. 2003). Mechie *et al*. (2009) estimate the depth to the Precambrian crystalline basement to be 11 km below sea level beneath the DESIRE wide-angle reflection/refraction (WRR) profile where it crosses the southern DSB.

The DEad Sea Integrated REsearch (DESIRE) project is a multinational, interdisciplinary geophysical initiative aimed at determining the crustal and upper mantle structure beneath the DSB. It consists of five sub-projects, namely plate movement, crustal structure that includes two controlled source seismic experiments (Mechie *et al*. 2009) and a natural source magnetotelluric experiment, aerogravity, earthquakes and radon, and geodynamic modelling. Here we describe a receiver function analysis of teleseismic records collected in the frame of the earthquakes and radon sub-project, in terms of crustal structure.

DATA

The passive seismological part of the DESIRE project, started in 2006 September. A temporary seismic network consisting of 24 broadband and 35 short period seismic stations (Fig. 2) was set up in the DSB area. Their coordinates are given in Table 1. These stations have been in operation between 2006 October and 2008 April. The aperture of the network is approximately 60 km in the E–W direction crossing the DSB on the Lisan peninsula and about 100 km in the N–S direction. Short period seismic stations were equipped with 1 Hz Mark L4 seismometers, whereas the broadband seismic stations were equipped with Guralp 40-T, 3-T and Streckeisen STS2 seismometers.

During the 18 months of successful operation, data were continuously sampled in the field at 100 and 200 Hz for the broadband and the short period seismic stations, respectively. The raw field data were converted to miniseed format and archived as full seed volumes

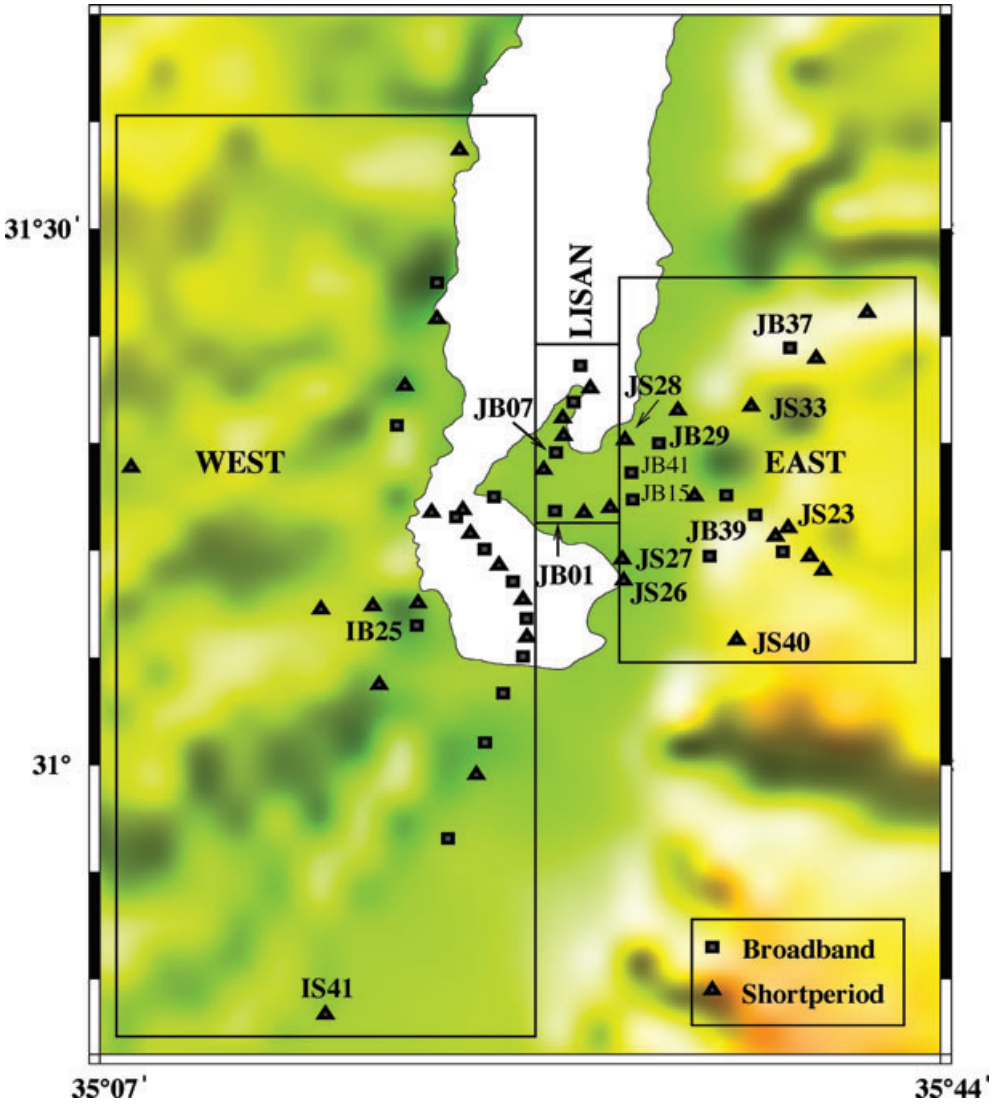

Figure 2. Location map of seismic stations in the region of the Dead Sea Basin. Stations are grouped into three regions: EAST, LISAN and WEST.

Table 1: Station codes and coordinates of earthquake stations of the DESIRE temporary network.

ID	Sensor	Latitude (°)	Longitude (°)
JB01	STS2	31.23710	35.47915
JB04	STS2	31.24997	35.42810
JS05	M-L4	31.23783	35.40220
JS06	M-L4	31.27531	35.46942
JB07	STS2	31.29146	35.47960
JS08	M-L4	31.30699	35.48604
JS09	M-L4	31.32339	35.48528
JB10	40-T	31.33855	35.49455
JS11	M-L4	31.35122	35.50832
JB12	STS2	31.37247	35.50018
JS13	M-L4	31.23487	35.50288
JS14	M-L4	31.23980	35.52475
JB15	40-T	31.24745	35.54355
JS17	M-L4	31.25093	35.59520
JB18	40-T	31.25148	35.62162
JB19	40-T	31.23319	35.64560
JS20	M-L4	31.21314	35.66253
JB21	STS2	31.19888	35.66875
JS22	M-L4	31.19445	35.69124
JS23	M-L4	31.22128	35.67334
JS24	M-L4	31.18134	35.70216
JS26	M-L4	31.17172	35.53622
JS27	M-L4	31.19172	35.53495
JS28	M-L4	31.30299	35.53738
JB29	40-T	31.30007	35.56571
JS31	M-L4	31.33068	35.58116
JS33	M-L4	31.33458	35.64223
JS35	M-L4	31.37906	35.69644
JS36	M-L4	31.42189	35.73890
JB37	STS2	31.38895	35.67463
JB39	STS2	31.19470	35.60761
JS40	M-L4	31.11655	35.63011
JB41	STS2	31.27262	35.54250
IS01	M-L4	31.27769	35.12615
IS08	M-L4	31.23533	35.37628
IB09	STS2	31.23122	35.39659
IS10	M-L4	31.21595	35.40861
IB11	40-T	31.20105	35.42019
IS12	M-L4	31.18602	35.43213
IB13	40-T	31.17122	35.44404
IS14	M-L4	31.15399	35.45222
IB15	STS2	31.13636	35.45527
IS16	M-L4	31.11923	35.45547
IB17	STS2	31.10100	35.45228
IB19	STS2	31.06688	35.43584
IB21	STS2	31.02075	35.42053
IB25	40-T	31.13022	35.36363
IS26	M-L4	31.14812	35.32716
IS27	M-L4	31.14518	35.28396
IB31	3-T	31.31658	35.34742
IS32	M-L4	31.35350	35.35403
IS34	M-L4	31.07471	35.33270
IS35	M-L4	30.99087	35.41338
IB36	STS2	30.93126	35.38962
IS37	M-L4	31.41615	35.38063
IB38	3-T	31.44987	35.38094
IS40	M-L4	31.15069	35.36510
IS41	M-L4	30.76707	35.28793
IS42	M-L4	31.57322	35.39954

in the GEOFON data centre of the GFZ, Potsdam/Germany. The data that have been used for this study, from three component seismic stations, were selected according to the following criteria.

(1) Only teleseismic earthquakes with epicentral distances ranging from 30° to 90° have been used to calculate receiver functions.

(2) Earthquakes with magnitudes greater than 5.6 and clear records of *P* onsets with high signal-to-noise ratio have been selected.

(3) Earthquakes within all depth ranges (shallow, intermediate and deep) were selected. A total number of about 90 useful teleseismic earthquakes according to the described criteria have been used in this study. The epicentres of the selected earthquakes are shown in Fig. 3, where most of the events are in the E and NE quadrants. For this study, the data have been filtered using a bandpass filter of 5–20 s.

RECEIVER FUNCTION TECHNIQUE

The receiver function method is a way to detect, isolate and enhance the *P*-to-*S* converted phases which are produced as teleseismic *P* waves cross a seismic discontinuity. *P*-to-*S* converted phases are used to image the crustal structure underneath seismic stations. A detailed description of the receiver function technique has been reported in a number of papers (e.g. Burdick & Langston 1977; Vinnik 1977; Owens *et al*. 1984; Ammon *et al*. 1990; Zandt & Ammon 1995; Owens *et al*. 2000) and it has been successfully applied for example in Germany (Kind *et al*. 1995; Grunewald *et al*. 2001), in Tibet (Yuan *et al*. 1997; Kind *et al*. 2002), in the Middle East (Hofstetter & Bock 2004; Mohsen *et al*. 2005), in north America (e.g. Ramesh *et al*. 2002) and in the Andes (Yuan *et al*. 2002). Here we briefly mention the processing steps applied. Each seismogram is rotated from the original Z, NS and EW components into the ray coordinate system L, Q and T. The L component points in the direction of the direct *P* wave, whereas the Q-component is perpendicular to the L component. The T component is perpendicular to both L and Q components. The L, Q and T components contain mainly the *P*, *SV* and *SH* energy, respectively. Receiver functions are calculated by the deconvolution of the *P* waveform on the L component from the Q and T components (Vinnik 1977). Deconvolution in the time domain has been used as described in Kind *et al*. (1995). It generates the inverse filter in the time domain by minimizing the least-squares difference between the observed seismogram and the desired delta-like spike function of normalized amplitude. The *P* waveform on the L component is used to generate the deconvolution filter. After deconvolution, all components are normalized to the maximum amplitude of the spike on the L component to preserve the absolute amplitude of conversion ratios. The deconvolution time window must be long enough so that most energy of the direct *P* wave is included. In the data processing in this study, the deconvolution window lengths are selected at 100 s. The time delay between the first arriving direct wave and an associated converted phase is a function of the discontinuity depth, the velocity structure of the medium above the discontinuity and the epicentral distance. Using the time difference between the PS phase and the first arrival, the depth to the discontinuity can be estimated based on the following equation (Kind & Vinnik 1988; Ravi Kumar & Bostock 2008):

$$tps = H\left(\left(V_s^{-2} - p^2\right)^{1/2} - \left(V_p^{-2} - p^2\right)^{1/2}\right),$$

where H is the depth to the discontinuity (e.g. Moho), *tps* is the delay time between the first arrival and the converted phase, V_s

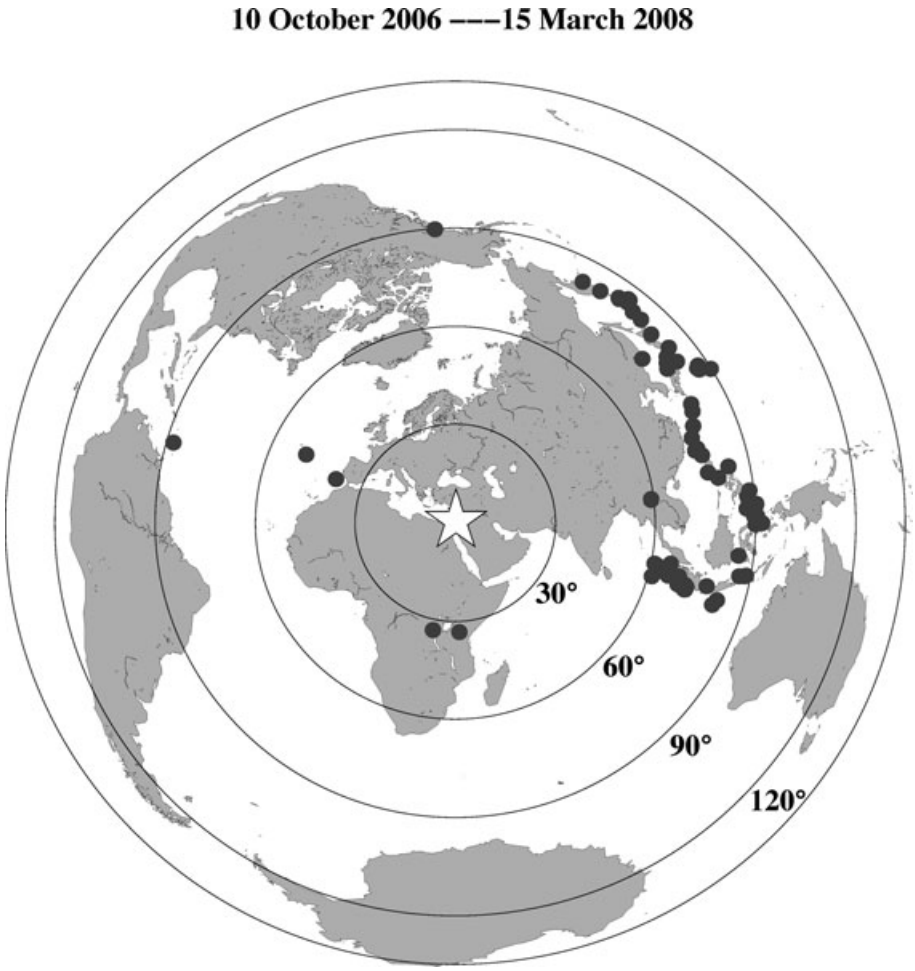

Figure 3. Distribution of teleseismic events with magnitude greater than 5.6 used in this study for receiver function analysis. The equidistant circles show distances in degrees to the DESIRE network in the Middle East.

is the *S*-wave velocity, V_p is the *P*-wave velocity and p is the ray parameter. To further improve the signal-to-noise ratio, we sum the rotated and deconvolved receiver functions from earthquakes over a wide range of distances (30°–90°) in the time domain. As the delay time of a converted phase depends on the slowness of the incident *P* wave and the discontinuity depth, we apply the moveout correction for the *P*-to-*S* converted phase relative to a reference slowness of 6.4 s per degree.

RECEIVER FUNCTION RESULTS

Examples of some individual seismic stations are plotted in Fig. 4(a)–(d), in a time window between 0 and 40 s, in which the direct conversions from the sediments, Moho and the crustal multiples are clearly visible. The abscissa represents the conversion time for PS with respect to the direct *P*-arrival time, commonly termed as 'delay time', and the sum trace is displayed on the top of each station panel.

Figs 4(a)–(d) show data examples for stations JB01, JB07, JB37 and IS41, respectively. Stations JB01 and JB07 (Figs 4a and b) are located on the Lisan peninsula in the DSB. Several phases are identified at these stations. The first one is a negative conversion labelled 'N', which is only visible at stations in the Lisan peninsula. Stations in the eastern part and the western part of the array do not have this negative phase. The arrival times for these stations are at 1 and 1.35 s, respectively. The second phase is a conversion from the Moho discontinuity labelled 'M' at 4.1 and 3.9 s, respectively. Crustal multiples labelled 'MM' are clearly seen. An additional positive phase at about 10 s delay time between the Moho and the Moho multiple is also clearly seen and labelled 'LCM'. This phase is probably caused by a discontinuity in the lower crust (as will be shown later). Such a phase was also identified in the earlier DESERT study east of the DST (Mohsen *et al*. 2005). Mohsen *et al*. (2005) inverted the waveforms using simple models with a maximum of four layers instead of the full inversion technique which generally results in many layers. When simple models are utilized each significant phase can be identified, although the waveform fit might not be as good as in the full inversion with many layers. Mohsen *et al*. (2005) studied the case in which the lower crustal discontinuity was at 29 km depth and the Moho was at 37 km depth and concluded that the Moho conversion is indeed a superposition of a conversion from the top of the 8-km-thick high-velocity lower crustal layer and the Moho. Even when the lower crustal discontinuity is moved up to midway between the base of the sediments at 3 km depth and the Moho at 37 km depth, the vertical resolution is not such that three separate converted phases can be observed and one has to rely on the recognition of the multiple from the lower crustal discontinuity to identify this discontinuity. A further fact that confirms that the phase at 10 s is a multiple can be clearly seen in Mohsen *et al*.

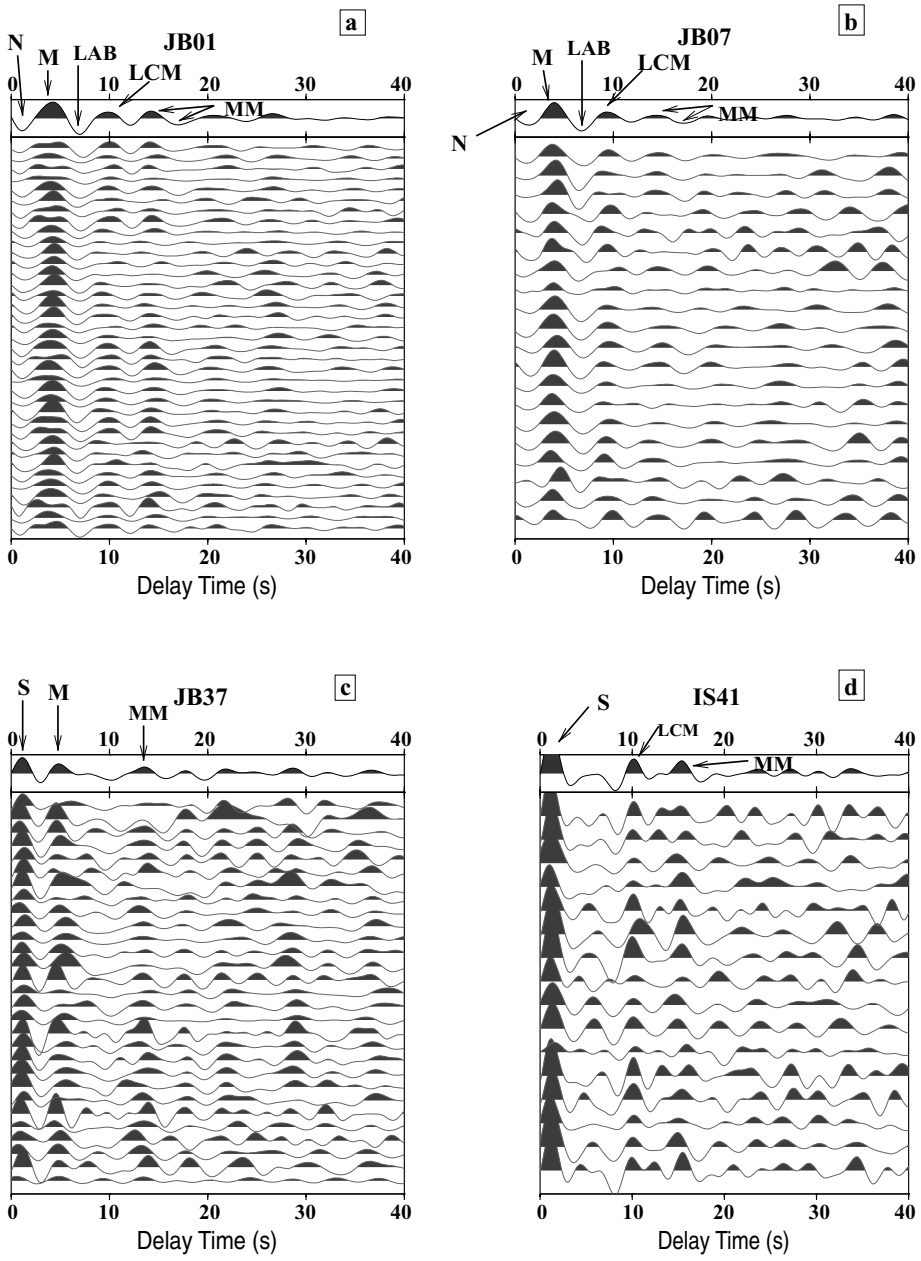

Figure 4. (a–d) Receiver functions for the stations JB01, JB07, JB37 and IS41 situated in the Dead Sea Basin area. The traces are moveout-corrected for PS conversions underneath the stations. The abscissa denotes the delay time with respect to the P-onset time. The upper panel in each figure represents the summation trace of the receiver functions. S represents the Sediment conversion, N represents a Negative conversion due to the basin structure, M represents the Moho conversion, MM represents Moho Multiples, LCM represents the Lower Crustal Multiple and LAB represents the lithosphere–asthenosphere boundary.

(2006), who used the *S* receiver function technique to study the thickness of the lithosphere east of the DST. Some of the piercing points at 80 km depth are located on the western side of the DST, where part of the DESIRE project is located. Here, no indication for a discontinuity at 10 s delay time has been observed (for more details concerning this multiple, see Mohsen *et al*. 2005 & 2006).

The negative phase that arrives directly after the Moho (e.g. JB01) possibly marks the seismic lithosphere–asthenosphere boundary (LAB). Fig. 5(a) shows the highpass filter for station JB01. It is clearly seen that this phase is a separate phase and not a side lobe. The data are also processed using the *S*-to-*P* receiver function technique (Fig. 5b) that was developed and applied by, for example Fara & Vinnik (2000), Yuan *et al*. (2006) and Mohsen *et al*. (2006). Low-velocity zones in the upper mantle usually derived using surface waves are frequently interpreted as the asthenosphere. Therefore, *S* receiver function observations of a negative discontinuity in the upper mantle are also explained as observations of the LAB. The converted phases arrive at the seismic station earlier than the direct *S* waves (precursors). The multiple reverberations appear later than the *S* arrival. This means that the *S* receiver function technique conveniently separates the primary *S*-to-*P* conversions from the later multiples of the *S* arrival. Similar to *P* receiver functions, the sign of the *S* receiver function signal is related to the velocity contrast across a discontinuity. Positive converted phases from the Moho indicate velocity increase with depth, whereas a negative phase indicates velocity decrease with depth. In Fig. 5(b), two phases are

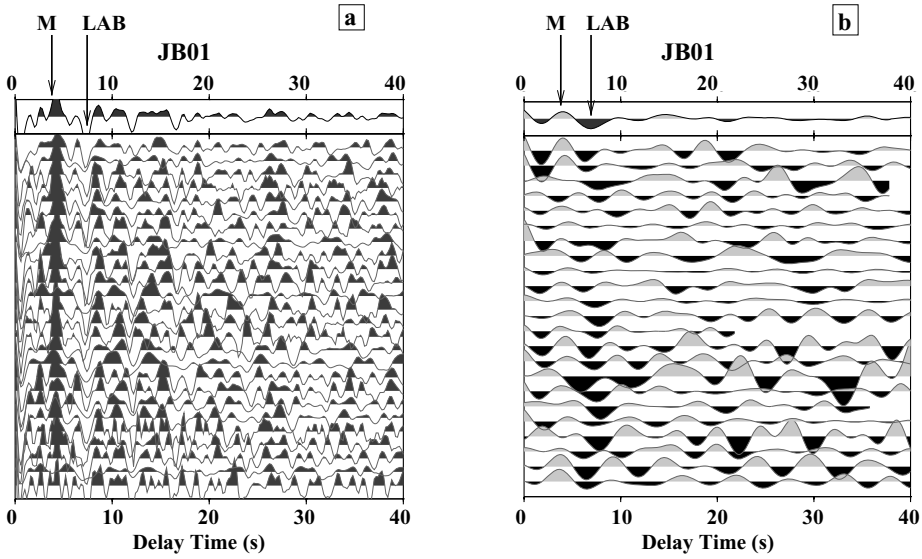

Figure 5. (a, b) Receiver functions of the station JB01 using *P*-to-*S* and *S-to-P* techniques, respectively. The left panel (a) shows the *P-to-S* receiver functions using a highpass 10 s filter. The right panel (b) shows the *S-to-P* receiver functions. In panel b, the *S* arrival time is at zero seconds, and the timescale is reversed for better comparison with the *P* receiver functions. The sum trace is displayed at the top. Two phases are visible, the positive Moho (M) and the negative lithosphere–asthenosphere boundary (LAB).

visible. The first is the positive Moho conversion at about 4 s and the second is the negative LAB conversion at about 7–8 s.

Fig. 4(c) shows data for station JB37. This station is located on the highlands of the eastern flank of the DSB. Phases are identified in the traces and marked in the summation trace. The first positive conversion labelled 'S', which originates from a strong contrast in the uppermost 10 km of the crust, is attributed to a thick sedimentary layer corroborated by other geological and geophysical studies in the area (Mechie *et al*. 2009). The traveltime for this station is 1.1 s. The second prominent positive phase is the conversion from the Moho discontinuity at 4.7 s. Crustal multiples generated between the Moho and the free surface arrive at around 14 s delay time. No additional phase at about 10 s has been noticed from stations on the eastern flank of the DSB, except for four stations named JB29, JB39, JS23 and JS40.

Fig. 4(d) shows data for station IS41 that is located in the southern part of the study area. Similar to the above-mentioned stations in the DSB and on the eastern flank of the basin, phases are identified in the traces and marked in the summation trace. Station IS41 shows a direct conversion in the uppermost 10 km of the crust (labelled S) followed by a positive phase, again labelled 'LCM', at about 10 s delay time. The conversion from the Moho is not seen on the summation trace and it seems that it is masked by multiples from the sediments present in the area. However, crustal multiples generated between the Moho and the free surface (labelled MM in Fig. 4d), arriving at 15–16 s delay time, are seen.

Seismic images derived from all seismic stations

Figs 6(a)–(e) show receiver functions of all seismic stations. The records are grouped according to the presence or absence of the negative phase and the multiple of the lower crustal discontinuity. Fig. 6(a) shows the receiver functions for all stations on the eastern flank of the DSB (see Fig. 2 for the location of the seismic stations). All traces are displayed according to the longitude of the stations from west to east. This figure shows clearly the following main features.

(1) A direct conversion at about 1 s labelled as 'S' and which is present all along this part of the transect from west to east. This phase is correlated with the sediments present in the area. The western part of this figure (A) shows the data from the stations located on the shoulder, close to the margin, of the Lisan peninsula. The stations are JS27, JS26, JS28, JB15 and JB41. They show a complexity of the area because of the effect of the basin. They show less than 0.4 s delay time in comparison with the other stations located further away from the basin on the eastern flank.

(2) A prominent positive conversion from the Moho at 4–5 s present all along this part of the profile and increasing from west to east.

(3) A positive peak at about 14 s is due to multiples between the Moho boundary and the free surface.

Figs 6(b) and (d) show the results from the stations located on the Lisan peninsula in the DSB (see Fig. 2 for the location of the seismic stations). The traces are sorted according to the latitude of the seismic stations, and the slowness, respectively. Figs 6(b) and (d) show the following features.

(1) A strong negative phase with more than 1 s delay time labelled as 'N' and which is present at all stations that are located on the Lisan peninsula. It will be shown below with 2-D modelling that the most plausible cause of this negative phase is the structure of the basin.

(2) A prominent positive phase from the Moho.

(3) Clear crustal multiples at about 14 and 18 s that are due to multiple reflections between the Moho boundary and the free surface.

(4) Another positive phase at about 10 s parallel to the Moho multiples is a coherent and strong phase, which is interpreted as a multiple of lower crustal origin as will be also shown in the 2-D modelling later. This phase is present at the stations on and to the west of the Lisan peninsula (regions Lisan and West in Fig. 2).

Figs 6(c) and (e) show the results from the last data set of the DESIRE stations in the western region (see Fig. 2 for the location of the seismic stations). The traces are sorted according to the latitude

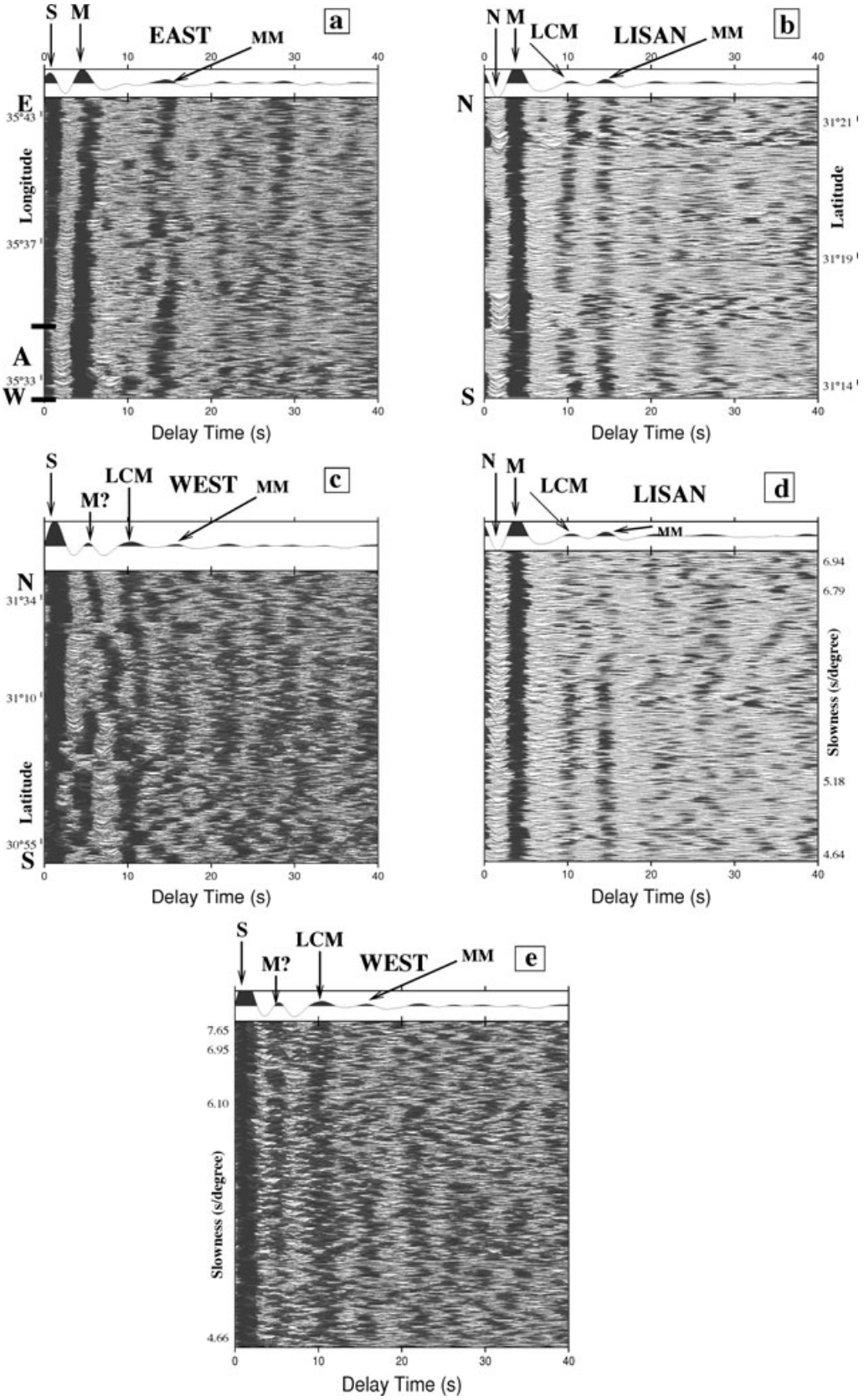

Figure 6. (a–e): Plot of all receiver functions of the DESIRE temporary network in three groups (EAST, LISAN and WEST). In a–c traces are plotted according to longitude and latitude, respectively, whereas in d–e the traces are plotted according to the slowness. The traces are moveout-corrected for PS conversions underneath the stations. Several crustal phases can be seen especially in the summation trace. S, sediments; N, Negative phase associated with the basin structure; M, Moho; MM, Moho multiples and LCM, lower crustal multiple.

of the seismic stations, and the slowness, respectively. Figs 6(c) and (e) show the following features.

(1) A strong conversion at more than 1 s, which is present at all the stations. This strong conversion is correlated with the thick sediments present in the area.

(2) A weak conversion from the Moho, that disappears at some locations because of the multiples from thick sediments. Conversion times from the thick sediments of 1.2–1.6 s are not unusual in this region. In these instances, times at which the sediment multiples can be expected range from 3.6 to 5.6 s, which is the same time as the Moho conversion.

(3) Crustal multiples can be identified, but they are not as strong as those at the stations in Figs 6(a), (b) and (d).

(4) The same positive phase at about 10 s as in Figs 6(b) and (d).

Traveltime maps

We have measured manually the times of the two main direct conversions (Sediments and Moho) and the LCM. Observed delay times were picked carefully at the highest amplitude of the phase which, in most cases, coincides with the symmetrical centre of the phase. The results of visual readings of the delay times for all DESIRE seismic stations are presented in Figs 7(a)–(c). Fig. 7(a) shows the distribution of the sediment delay times. It clearly shows an increase in the DSB and decrease to the east. Models of the *P*-wave velocity structure derived from the WRR data show that the sedimentary infill associated with the formation of the southern DSB is about 8.5 km thick beneath the profile with an additional 2 km of older sediments, resulting in the depth to the seismic basement beneath the southern DSB being about 11 km below sea level beneath the profile (Fig. 1) (Mechie *et al*. 2009). Seismic refraction data from

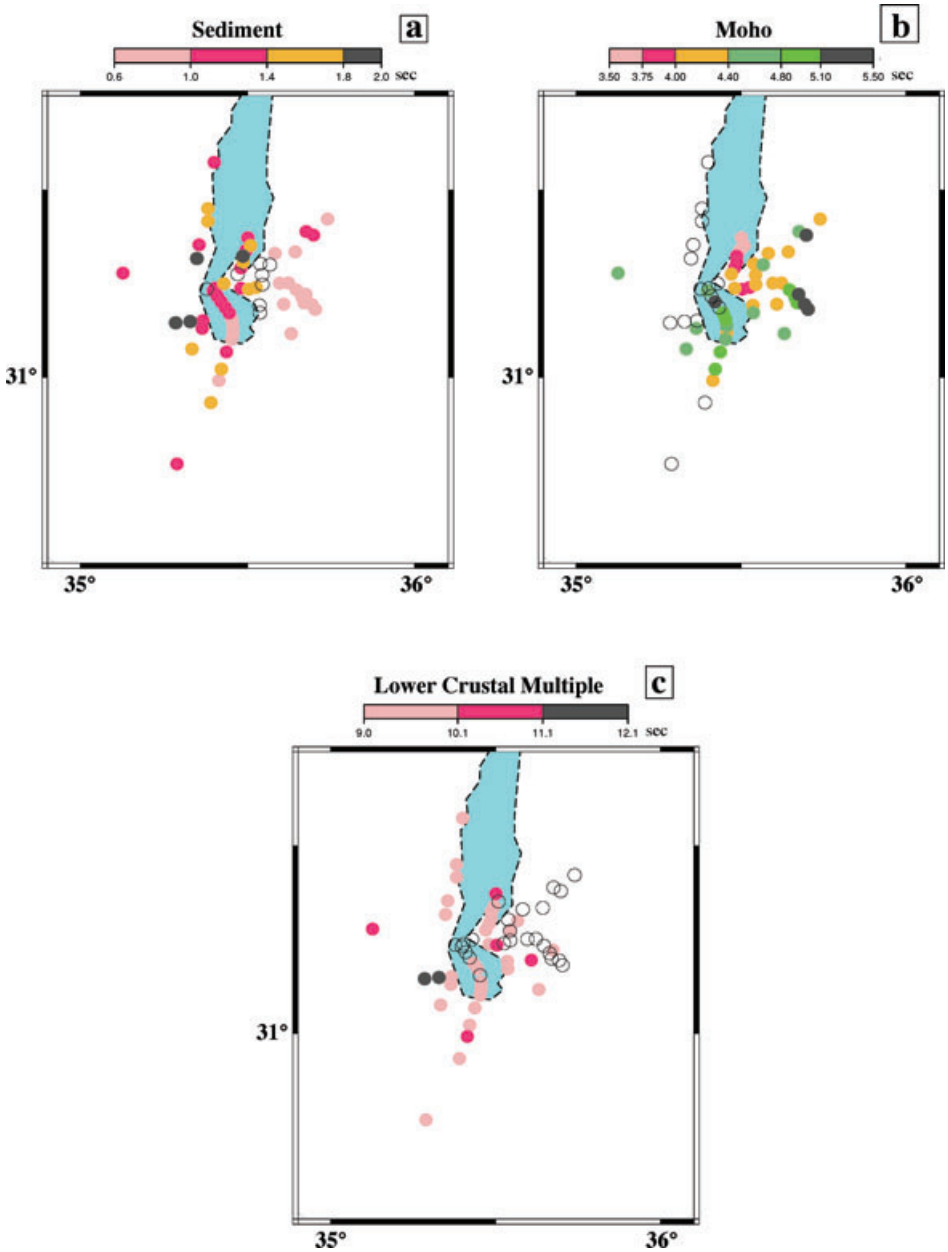

Figure 7. (a–c): Delay time maps for the first conversion from the sediments and the Moho, and the lower crustal multiple for all DESIRE seismic stations. Open circles represent stations that were difficult to pick. The colour code is in sec delay time with respect to *P*.

an earlier experiment suggest that, the seismic basement continues deeper to a maximum depth of about 14 km, about 10 km south of the DESIRE profile. This is in good agreement with our results. Fig. 7(b) shows the distribution of the Moho delay times. It shows a clear decrease of Moho delay times in the Lisan peninsula and an increase to the east. However, at about 20 per cent of the stations the Moho delay time is not easily picked and these stations are represented by open circles in the map. Various geophysical studies have been carried out in different parts of the DST region, such as seismic reflection/refraction profiles (Makris *et al*. 1983; El-Isa *et al* 1987a, 1987b; DESERT Group 2004; Mechie *et al*. 2005; Mechie *et al*. 2009), local source (Koulakov & Sobolev 2006) and teleseismic tomography (Koulakov *et al*. 2006) as well as gravity studies (Al-Zoubi & Ben-Avraham 2002; Götze *et al*. 2006). Receiver functions (Hofstetter & Bock 2004; Mohsen *et al*. 2005) have provided information about the crustal structure in the Araba fault region. Most of these studies suggest that the crustal thickness varies from about 30 km in the west to about 38 km in the east. The crustal thickness in this study region, including the DSB, is about 30–38 km, with the central part, the Lisan, having the smallest crustal thickness. To transform the time domain into the depth domain, the *P*- and *S*-wave velocity models for the DESIRE wide-angle reflection/refraction profile (Mechie *et al*. 2009) have been used.

Obvious evidence of an intra-crustal phase is found on and to the west of the Lisan peninsula with an average delay time of about 10 s (Fig. 7c). In the DESERT project, a lower crustal reflector was observed from the near vertical reflection (NVR) data, rising from the Moho at the DST to less than 30 km towards the east (DESERT Group 2004). The same feature is observed also from receiver function results at the DST and to the east of it within the same depth range. No similar feature is observed west of the DST along the DESERT profile (DESERT Group 2004; Mohsen *et al*. 2005). However, noting that the DESERT profile crosses the DST about 100 km south of the DESIRE profile and removing the 107 km of left-lateral movement along the DST, then the structure east of the DST beneath the DESIRE region should only have been a few kilometres south of the structure west of the DST below the DESERT region, before movement along the DST started (Fig. 8). Neglecting the few kilometres difference one indeed sees that both east of the DST beneath the DESIRE region and west of the DST beneath the DESERT region, there is no lower crustal multiple observed in the receiver function data. The regions where a lower crustal multiple is observed represent regions approximately 100 km north and south of the region where no lower crustal multiple was present before movement along the DST began 18 Ma ago (Quennell 1958; Garfunkel 1981). These regions most probably cross the DST at quite a high angle, otherwise the structural pattern that is recognized would not be observed as such. The most likely candidates for such structures are those related to the formation of the Arabian Shield in Precambrian times. Some of the major terrane boundaries in the present-day Arabian Shield are oriented NW–SE (Stern & Johnson 2010) and could thus be likely candidates for explaining the receiver function observations of this and the DESERT study. It can be imagined that there existed at 18 Ma ago a terrane which has no lower crustal discontinuity separating two terranes to the north and south, both of which do have such a discontinuity. Another possibility could be structures associated with the Tethys passive margin. However, this possibility is thought to be less likely as the margin runs more or less parallel to the DST in the study area.

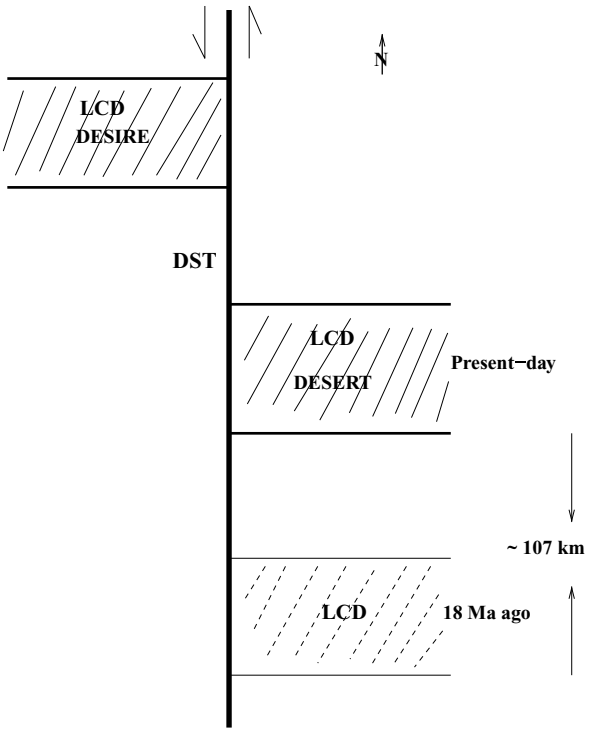

Figure 8. Sketch showing where the lower crustal discontinuity (LCD) is present or absent in the vicinity of the Dead Sea Transform (DST) both 18 Ma ago and at the present-day.

2-D modelling

To examine the effects of the DSB, 2-D waveform modelling was carried out along a profile perpendicular to the trend of the DSB. This can be justified as many of the earthquakes used in this study are more or less in line with this profile. Earthquakes which are significantly off-line were not included in the comparison between observed data and synthetic data generated from the 2-D modelling. Synthetic waveforms were calculated using a finite-difference approximation of the wave equation for 2-D heterogeneous elastic media by Kelly *et al*. (1976) with transparent boundary conditions (Reynolds 1978) and implemented by Sandmeier (1990). In this study, the 2-D models were sampled at 400 m spacing in both the horizontal and vertical directions, which allowed seismograms with a dominant period of 3 s to be calculated. The seismograms were calculated in response to a plane wave arriving either from the east or the west with an angle of incidence of 27° at the base of the model. The synthetic data were processed in exactly the same manner as the observed data to obtain synthetic receiver functions.

More than 35 models have been calculated. The model which through visual inspection seems to fit the data best (Fig. 9) comprises a basin 15–20 km wide and about 10 km deep, a high *S* velocity lower crustal layer beneath and west of the basin and a 2 km shallower Moho beneath the basin. In keeping with seismic wide-angle reflection/refraction results in the region (ten Brink *et al*. 2006; Mechie *et al*. 2009), the boundary between the upper and lower crust has been modelled as a prominent discontinuity beneath the whole profile. With this type of structure, the main features in the receiver functions can be reproduced, for example the negative phase and the somewhat smaller delay times for the Moho conversion at the stations on the Lisan peninsula and the LCM at stations

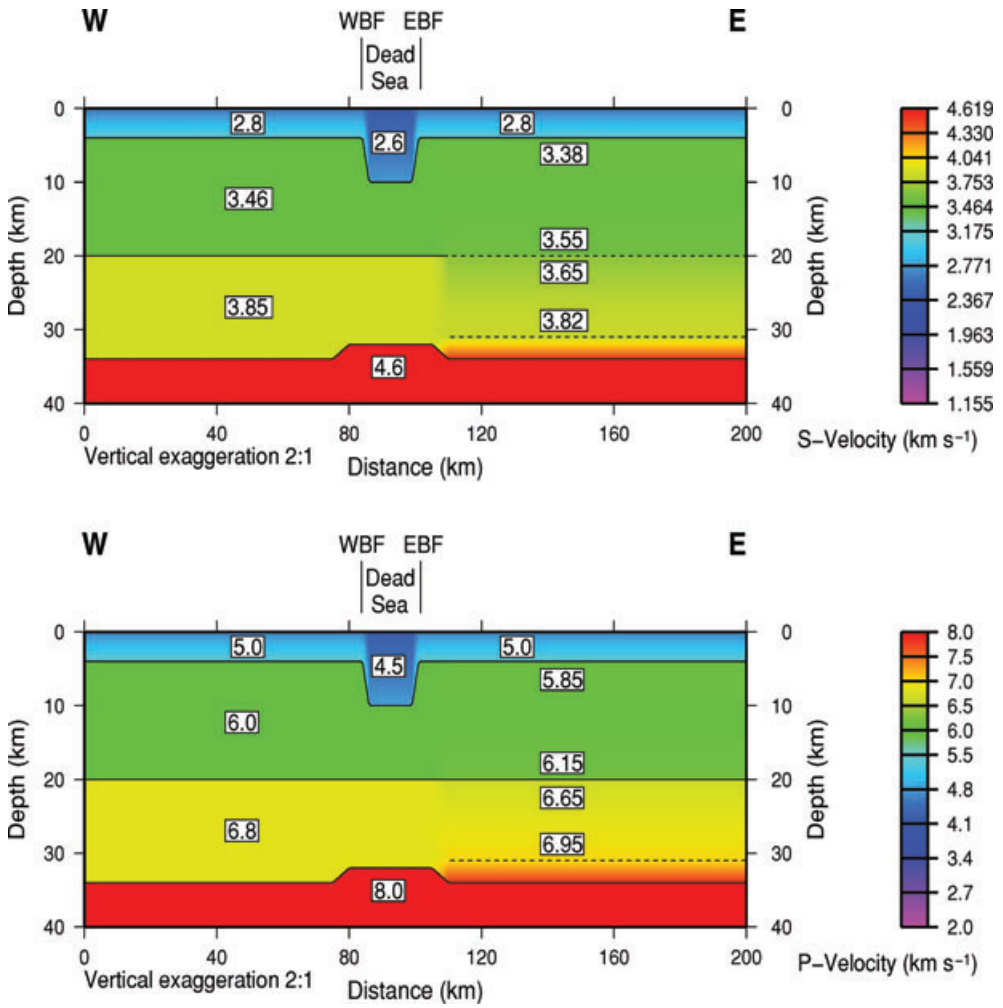

Figure 9. Two dimensional *P*- and *S*-wave velocity models used to generate synthetics of converted phases and their multiples. Intracrustal boundaries at which the velocity jump does not exceed 0.1 km s^{-1} are marked as dashed lines. For the boundary at 20 km depth east of the Dead Sea basin, this means that a significant *P*-to-*S* conversion and hence a significant lower crustal multiple (LCM) are not produced. The transition from mantle to crustal velocities over a depth range of 3 km at the Moho east of the Dead Sea basin means that a significant *P*-to-*S* conversion is produced as well as recognizable Moho multiples. Key: WBF, Western Boundary Fault; EBF, Eastern Boundary Fault.

within and west of the Lisan peninsula (Fig. 10). In particular, it can be noted that as soon as a basin-like structure is introduced into the model then, for sources from the east, the negative phase appears at stations that are a similar distance west of the eastern margin of the basin in the model, as the stations on the Lisan peninsula are away from the major fault bounding the eastern side of the DSB. Thus, an explanation for the negative phase in the observed data is provided without resorting to a low velocity zone. If 1-D modelling only had been utilized in this study, then a high S velocity of 3.5–3.8 km s^{-1} would have been required in the upper 10 km below the Lisan peninsula, followed by a very significant velocity reduction of 0.7–1 km s^{-1}, to explain this phase. Such a velocity structure is unlikely in this region where the Lisan salt diapir of Pliocene age exists. For sources from the west there are only suitable observed data from station JB39 east of the DSB. For this station, a lower crustal multiple is produced in the synthetic data for a station a similar distance east of the eastern margin of the basin in the model as station JB39 is from the major fault bounding the eastern side of the DSB. On the other hand, station JB39 is one of the few stations east of the DSB, which generally exhibits the LCM. For sources from the west, one has to go about 15–20 km east of the edge of the prominent discontinuity in *S* velocities at 20 km depth, before the LCM signal essentially disappears. Taking into account the incidence angle of the incoming wave, this is about 10–15 km further than predicted by ray theory for high frequencies. A further consequence of the model due to the fact that the LCM is not observed to the east of the DSB is an E–W change in Poisson's ratio. For the lower crust alone Poisson's ratio changes from 0.28 east of the DSB to 0.26 west of the Eastern Boundary Fault (EBF, Fig. 10). However, for the whole crust this means a change in Poisson's ratio of less than 0.01.

CONCLUSIONS

The results presented earlier and those of earlier studies suggest that the crustal thickness is about 30–38 km from the Mediterranean Sea to the highlands in Jordan crossing the DSB. Refraction, reflection, receiver functions and gravimetric studies show the Moho is shallower near the Mediterranean Sea and increases towards the highlands in Jordan. In this study, results from different seismic

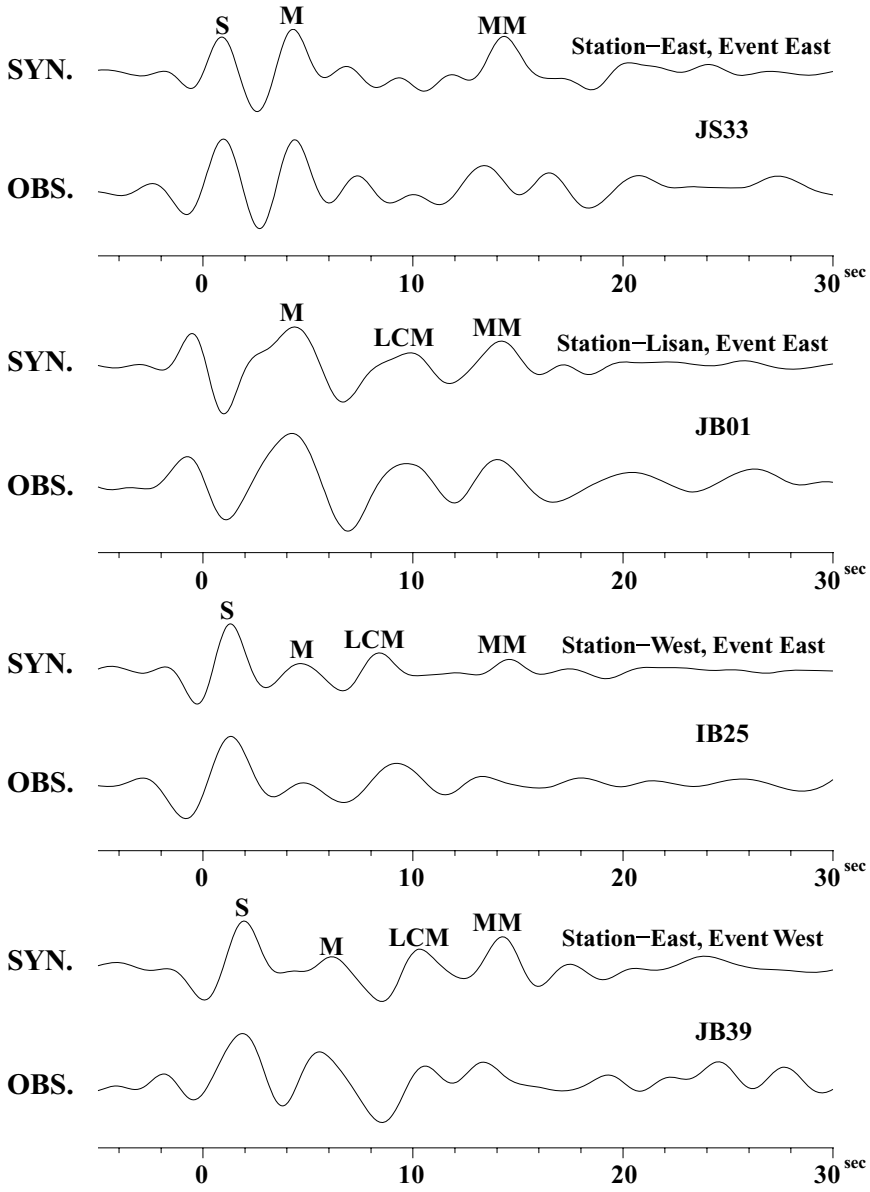

Figure 10. Comparison between the synthetic and the observed receiver functions. The synthetic traces are calculated with a 2-D finite-difference method. There are examples for stations from all three groups, West, Lisan and East for waves arriving from the east and for the eastern group for waves arriving from the west. S, sediments; M, Moho; MM, Moho multiples; LCM, lower crustal multiple.

techniques are compared to better understand the crustal structure across the DSB. These include near-vertical incidence and wide-angle (NVR and WRR) controlled-source techniques along a linear profile perpendicular to the DSB and the natural source–receiver function technique. A comparison is shown for depths to the seismic basement, and depths to the Moho between these seismic experiments (Fig. 11). The receiver function results agree with those obtained from the WRR profile. For stations in the DSB delay times are more than 1 s, while east of the DSB they are less than 1 s except for two stations. Transforming the time domain into the depth domain gives an 8–10 km depth beneath the DSB and about 10 km from the 2-D modelling. The depth to the basement in the eastern part is about 3–4 km. The Moho depths in terms of travel-times show that the Moho is shallower below the Lisan peninsula and increases to the east. The 2-D model includes Moho depths that are about 2 km shallower under the DSB and increase to the east. However, an additional positive phase at about 10 s delay time between the Moho conversion and the Moho multiple is also clearly seen in the DSB and in a N–S profile west of the basin. It is indicated that this phase is a multiple from a lower crustal discontinuity because it arrives parallel to the Moho multiple. The same phase was found at 10 s also in Wadi Araba east of the Dead Sea Transform (DESERT Group 2004; Mohsen *et al*. 2005). The two directly converted phases from the lower crust and the Moho cannot be separated due to their relatively long periods and small differential times. As indicated earlier, before the 107 km left-lateral movement along the DST began 18 Ma ago, the region beneath the DESIRE array where the lower crustal discontinuity is observed lay about 200 km north of the region below the DESERT array where this discontinuity is recognized. A region where no lower crustal

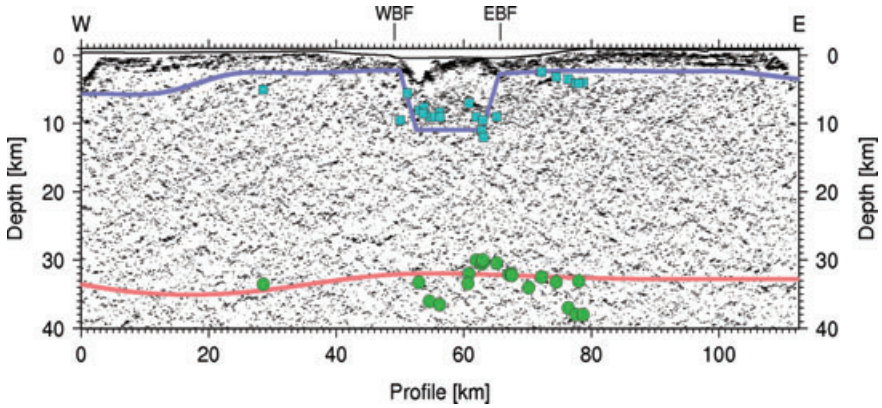

Figure 11. Comparison of depth determinations for the sediments and the Moho between the near-vertical incidence and wide-angle controlled-source techniques and receiver functions. For the receiver functions, the error in the Moho depth is about 3 km and is about 1 km for the basement depth. The red and blue lines represent the depths to the Moho and the basement, respectively, obtained by the wide-angle experiment (Mechie *et al*. 2009). Green circles and blue squares are the values obtained from receiver functions for the Moho and the basement, respectively. There is no Moho observed in the near-vertical incidence data. Key: See Fig. 9.

discontinuity is observed lay between these two regions about 18 Ma ago (Fig. 8).

ACKNOWLEDGMENTS

The DESIRE project was funded by the Deutsche Forschungsgemeinschaft. Al-Najah National University in Nablus, Palestine, the Natural Resources Authority of Jordan and the National Ministry of Infrastructure of Israel are thanked for support. The instruments were provided by the Geophysical Instrument Pool of the Deutsches GeoForschungsZentrum Potsdam (GFZ). The following persons are acknowledged for their participation in the fieldwork of the passive experiment: S. Al-Qur'an, W. Abdelhafez, B. Al-Biss, H. Al Wahsh, M. Hijazi, A. Amrat, O. Mayyas, B. Heit, B. Braeuer, W. Berjoos, A. Abou Naser, M. Melkawi, and A. Khamees.

REFERENCES

Abou Karaki, N., 1987. Synthese et carte seismoteconique des pays la bordure orientate da la Mediterranee: Sismicite du system de failles du Jourdain-MerMorte. *PhD thesis*, IPGS, University Strasborg.

Alderson, F., Ben-Avraham, Z., Hofstetter, A., Kissling, E. & Al-Yazjeen, T., 2003. Lower crustal strength under the Dead Sea basin derived from local earthquake data and rheological modelling, *Earth planet. Sci. Lett.,* **214,** 129–142, doi:10.1016/S0012-821X(03)00381-9.

Al-Zoubi, A. & Ben-Avraham, Z., 2002. Structure of the Earth's crust in Jordan from potential field data, *Tectonophysics,* **346,** 45–59.

Al-Zoubi, A. & ten Brink, U., 2001. Salt diapirs in the Dead Sea Basin and their relationship to Quaternary extensional tectonics, *Mar. Pet. Geol.,* **18,** 779–797, doi:10.1016/S0264-8172(01)00031-9.

Al-Zoubi, A., Shulman, H. & Ben-Avraham, Z., 2002. Seismic reflection profiles across the southern Dead Sea basin, *Tectonophysics,* **346,** 59–67.

Ambraseys, N., Melville, R. & Adams, R., 1994. *The Seismicity of Egypt, Arabia and the Red Sea. A Historical Review*. Cambridge University Press, Cambridge, 181 pp.

Ammon, C.J., Randhall, C.E. & Zandt, G., 1990. On the nonuniqueness of receiver function inversion, *J. geophys. Res.,* **95,** 15303–15318.

Ben-Avraham, Z. & Schubert, G., 2006. Deep ''drop down'' basin in the southern Dead Sea, *Earth planet. Sci. Lett.,* **251,** 254–263.

Burdick, L.J. & Langston, C.A., 1977. Modelling crust-structure through the use of converted phases in teleseismic body-wave-forms, *Bull. seism. Soc. Am.,* **67,** 677–691.

DESERT Group, 2004. The crustal structure of the Dead Sea Transform, *Geophys. J. Int.,* **156,** 655–681.

El-Isa, Z.H., 1990. Lithospheric structure of the Jordan Dead Sea Transform from earthquake data, *Tectonophysics,* **180,** 29–36.

El-Isa, Z., Mechie, J., Prodehl, C., Makris, J. & Rihm, R., 1987a. A crustal structure study of Jordan derived from seismic refraction data, *Tectonophysics,* **138,** 235–253.

El-Isa, Z., Mechie, J. & Prodehl, C., 1987b. Shear velocity structure of Jordan from explosion seismic data, *Geophys. J. R. astr. Soc.*, **138,** 265–281.

Enzel, Y., Agnon, A. & Stein, M., eds, 2006. *New Frontiers in Dead Sea Paleoenvironmental Research,* Geological Society of America Special Paper, Vol. 401, Geol. Soc. Am., Boulder, CO, 253 pp.

Fara, V. & Vinnik, L., 2000. Upper mantle stratification by P and S receiver functions, *Geophys. J. Int.,* **141,** 699–712.

Frieslander, U. & Ben-Avraham, Z., 1989. Magnetic field over the Dead Sea and its vicinity, *Mar. Pet. Geol.* **6,** 148–160.

Garfunkel, Z., 1981. Internal structure of the Dead Sea leaky transform (rift) in relation to plate kinematrics, *Tectonophysics,* **80,** 81–108.

Garfunkel, Z. & Ben-Avraham, Z., 1996. The structure of the Dead Sea basin, *Tectonophysics,* **266,** 155–176.

Garfunkel, Z., Zak, I. & Freund, R., 1981. Active faulting along the Dead Sea Rift, *Tectonophysics,* **80,** 1–26.

Ginzburg, A., & Ben-Avraham, Z., 1997. Seismic refraction study of the northern basin of the Dead Sea, *Geophys. Res. Lett.* **24,** 2063–2066.

Girdler, R. W., 1990. The Dead Sea transform fault system. *Tectonophysics,* **180,** 1–13

Götze, H.J., El-Kelani, R., Schmidt, S., Rybakov, M., Förster, H.J. & Ebbing, J., 2006. Integrated 3-D density modelling and segmentation of the Dead Sea Transform, *Int. J. Earth Sci.,* **96,** doi:10.1007/s00531-006-0095-5.

Grunewald, S., Weber, M. & Kind, R., 2001. The upper mantle under Central Europe: indications for the Eifel plume, *Geophys. J. Int.,* **147,** 590–601.

Hofstetter, R. & Bock, G., 2004. Shear-wave velocity structure of the Sinai sub-plate from receiver function analysis, *Geophys. J. Int.,* **158,** 67–84.

Kashia, E. L. & Croker, P. F., 1987. Structural geology and evolution of the Dead Sea – Jordan rift system as deduced from new subsurface data, *Tectonophysics,* **141,** 33–60.

Kelly, K.R., Ward, R.W., Treitel, S. & Alford, R.M., 1976. Synthetic seismograms: a finite difference approach, *Geophysics,* **41,** 2–27.

Kind, R. & Vinnik, L.P., 1988. The upper mantle discontinuities underneath the GRF array from P-to-S converted phases, *J. Geophys.* **62,** 138–147.

Kind, R., Kosarev, G.L. & Petersen, N.V., 1995. Receiver functions at the stations of the German Regional Seismic Network (GRSN), *Geophys. J. Int.,* **121,** 191–202.

Kind, R. *et al.*, 2002. Seismic images of crust and upper mantle beneath Tibet: evidence for Eurasian plate subduction, *Science,* **298,** 1219–1221.

Koulakov, I. & Sobolev, S.V., 2006. Moho depth and 3 D P and S structure of the crust and uppermost mantle in the Eastern Mediterranean and Middle

East derived from tomographic inversion of local ISC data, *Geophys. J. Int.,* **164,** 218–235.

Koulakov, I., Sobolev, S.V., Weber, M., Oreshin, S., Wylegalla, K. & Hofstetter, R., 2006. Teleseismic tomography reveals no signature of the Dead Sea Transform in the upper mantle structure, *EPSL,* **252,** doi:10.1016/j.epsl.2006.09.39.

Larsen, B.D., Ben-Avraham, Z. & Shulman, H., 2002. Fault and salt tectonics in the southern Dead Sea Basin, *Tectonophysics,* **346,** 71–90, doi:10.1016/S0040-1951(01)00229-3.

Makris, J., Ben-Avraham, Z., Behle, A., Ginzburg, A., Giese, P., Steinmetz, L., Whitmarsh, R. & Eleftheriou, S., 1983. Seismic refraction profiles between Cyprus and Israel and their interpretation, *Geophys. J. R. astr. Soc.,* **75,** 575–591.

Mechie, J., Abu-Ayyash, K., Ben-Avraham, Z., El-Kelani, R., Mohsen, A., Rümpker, G., Saul, J. & Weber, M., 2005, Crustal shear velocity structure across the Dead Sea Transform from 2-D modelling of project DESERT explosion seismic data, *Geophys. J. Int.*, **160,** 910–924.

Mechie, J., Abu-Ayyash, K., Ben-Avraham, Z., El-Kelani, R., Qabbani, I., Weber, M. & DESIRE Group, 2009. Crustal structure of the southern Dead Sea basin derived from project DESIRE wide-angle seismic data, *Geophys. J. Int.*, **178,** 457–478.

Mohsen, A., Hofstetter, R., Bock, G., Kind, R., Weber, M., Wylegalla, K., Rümpker, G. & DESERT Group, 2005. A receiver function study across the Dead Sea Transform, *Geophys. J. Int.,* **160,** 948–960.

Mohsen, A., Kind, R., Sobolev, S., Weber, M. & DESERT Group, 2006. Thickness of the lithosphere east of the Dead Sea Transform, *Geophys. J. Int.,* **167,** 845–852.

Neev, D. & Hall, J.K., 1979. Geophysical investigations in the Dead Sea, *Sedimentary Geol.* **23,** 209–238.

Owens, T.J., Nyblade, A.A., Gurrola, H. & Langston, C.A., 2000. Mantle transition zone structure beneath Tanzania, East Africa, *Geophys. Res. Lett.,* **27,** 827–830.

Owens, T.J., Zandt, G. & Taylor, S.R., 1984. Seismic evidence for an ancient rift beneath the Cumberland Plateau, Tennesse: a detailed analysis of broadband teleseismic P waveforms, *J. Geophys. Res.,* **89,** 7783–7795.

Petrunen, A. & Sobolev, S., 2006. What controls thickness of sediments and lithospheric deformation at a pull-apart basin? *Geology,* **34,** 389–392.

Quennell, A.M., 1958. *The Structural and Geomorphic Evolution of the Dead Sea Rift,* The Geological Society of London, London.

Ramesh, D.S., Kind, R. & Yuan, X., 2002. Receiver function analysis of the North American crust and upper mantle, *Geophys. J. Int.,* **150,** 91–108.

Ravi Kumar, M. & Bostock, M.G., 2008. Extraction of absolute P velocity from receiver functions, *Geophys. J. Int.,* **175,** 515–519.

Reynolds, A.C., 1978. Boundary conditions for the numerical solution of wave propagation problems, *Geophysics,* **43,** 1099–1110.

Sandmeier, K.-J., 1990. Untersuchung der Ausbreitungsseigenschaften seismischer Wellen in geschichteten und streuenden Medien, *PhD thesis*, Karlsruhe University.

Smit, J., Brun, J.P., Cloetingh, S. & Ben-Avraham, Z., 2008. Pull-apart basin formation and development in narrow transform zones with application to the Dead Sea Basin, *Tectonics,* **27,** TC6018, doi:10.1029/2007TC002119.

Stern, R.J., & Johnson, P., 2010. Continental lithosphere of the Arabian Plate: A geologic, petrologic, and geophysical synthesis. *Earth Sci. Rev.,* **101,** 29–67.

ten Brink, U.S., Al-Zoubi, A.S., Flores, C.H., Rotstein, Y., Qabbani, I., Harder, S.H. & Keller, G.R., 2006. Seismic imaging of deep low-velocity zone beneath the Dead Sea basin and transform fault: implications for strain localization and crustal rigidity, *Geophys. Res. Lett.,* **33,** L24314, doi:10.1029/2006GL027890.

ten Brink, U.S., Ben-Avraham, Z., Bell, R.E., Hassouneh, M., Coleman, D.F., Andreasen, G., Tibor, G. & Coakley, B., 1993. Structure of the Dead Sea pull-apart basin from gravity analysis, *J. geophys. Res.,* **98,** 21 877–21 894.

ten Brink, U.S. *et al*. 1999. Anatomy of the Dead Sea Transform: does it reflect continuous changes in plate motion? *Geology,* **27,** 887–890.

Vinnik, L.P., 1977. Detection of waves converted from P to SV in the mantle, *Phys. Earth planet., Int.,* **15,** 39–45.

Yuan, X., Ni, J., Kind, R., Mechie, J. & Sandvol, E., 1997. Lithospheric and upper mantle structure of southern Tibet from a seismological passive source experiment, *J. geophys. Res.,* **102,** 27491–27500.

Yuan, X., Kind, R., Li, X., & Wang, R., 2006. The S receiver functions: synthetics and data examples, *Geophys. J. Int.,* **165**(2), 555–564, doi:10.1111/j.1365-246X.2006.02885.x.

Yuan, X., Sobolev, S.V. & Kind, R., 2002. Moho topography in the central Andes and its geodynamic implications, *Earth planet. Sci. Lett.,* **199,** 389–402.

Zandt, G. & Ammon, C.J., 1995. Continental crust composition constrained by measurements of crustal Poisson's ratio, *Nature,* **374,** 152–154.